

1 **Dangling bonds in a-Si:H revisited: A combined Multifrequency**
2 **EPR and DFT Study**

3 M. Fehr,* A. Schnegg, B. Rech, and K. Lips
4 *Helmholtz-Zentrum Berlin für Materialien und Energie,*
5 *Institut für Silizium-Photovoltaik, Kekuléstr. 5, 12489 Berlin, Germany*

6 O. Astakhov and F. Finger
7 *Forschungszentrum Jülich, Institut für Energie- und Klimaforschung,*
8 *Photovoltaik, 52425 Jülich, Germany*

9 G. Pfanner, C. Freysoldt, and J. Neugebauer
10 *Max-Planck-Institut für Eisenforschung GmbH,*
11 *Max-Planck Strasse 1, 40237 Düsseldorf, Germany*

12 R. Bittl and C. Teutloff†
13 *Freie Universität Berlin, Fachbereich Physik,*
14 *Arnimallee 14, 14195 Berlin, Germany*

15 (Dated: November 8, 2021)

Abstract

Multifrequency pulsed electron paramagnetic resonance (EPR) spectroscopy using S-, X-, Q- and W-Band frequencies (3.6, 9.7, 34, and 94 GHz, respectively) was employed to study paramagnetic coordination defects in undoped hydrogenated amorphous silicon (a-Si:H). The improved spectral resolution at high magnetic field reveals a rhombic splitting of the g-tensor with the following principal values: $g_x = 2.0079$, $g_y = 2.0061$ and $g_z = 2.0034$ and shows pronounced g-strain, i.e., the principal values are widely distributed. The multifrequency approach furthermore yields precise ^{29}Si hyperfine data. Density functional theory (DFT) calculations on 26 computer-generated a-Si:H dangling-bond models yielded g-values close to the experimental data but deviating hyperfine interaction values. We show that paramagnetic coordination defects in a-Si:H are more delocalized than computer-generated dangling-bond defects and discuss models to explain this discrepancy.

¹⁶ PACS numbers: 76.30.Mi,71.55.Jv,71.15.Mb

¹⁷ Keywords: electron paramagnetic resonance; defects; dangling bond; amorphous silicon; hydrogenated amor-
¹⁸ phous silicon; density functional theory; g value; hyperfine interaction

19 I. INTRODUCTION

20 The performance of thin-film solar cells and other devices based on hydrogenated amor-
21 phous silicon (a-Si:H) is limited by localized defect states in the mobility gap, which act as
22 recombination centers for excess charge carriers. In undoped a-Si:H, the defect centers are
23 often paramagnetic and give rise to an inhomogeneously broadened asymmetric EPR line at
24 around $g = 2.0050 - 2.0055$ ¹. The intensity of this signal is routinely used as a measure for
25 the electronic quality of a-Si:H². The impact of these defect centers on the efficiency of solar
26 cells is even aggravated by the fact that the defect density significantly increases upon light
27 exposure³. This light-induced degradation phenomenon, known as the Staebler-Wronski ef-
28 fect (SWE)^{4,5}, significantly limits the maximum efficiency of solar cells based on a-Si:H⁶.
29 In order to reduce the impact of a-Si:H defects in the degraded state optimized deposition
30 protocols have been developed⁷. Despite these improvements, a nanoscopic understanding
31 of the processes leading to the creation of light-induced defects is still missing⁶. Detailed
32 knowledge about the microscopic origin of SWE defects leading to strategies to eliminate
33 them is therefore mandatory to reach ultimate device performance. Moreover, knowledge of
34 the detailed structure of the defect and the distribution of H atoms in its vicinity is of main
35 importance for the models for the SWE. In view of the latest EPR experiments it became
36 evident that in as grown materials the H is randomly distributed with respect to the defect
37 center⁸. If hydrogen is mediating the SWE effect, it is important to find the precursor of
38 such a state.

39 There is a general consensus in the research community that the dominating defects in a-
40 Si:H are intrinsic coordination defects, i.e. over- (fivefold) or undercoordinated (threefold)
41 Si atoms. The latter are usually denoted by dangling-bond (DB) defects. To conclude on
42 the defect structure, EPR techniques are most valuable, since the EPR spectrum reflects
43 the electronic structure of the paramagnetic defect. In the present case, the EPR spectrum
44 is determined by two interactions, the Zeeman interaction given by the g-tensor, and the
45 hyperfine interaction (HFI) between the unpaired electron spin and nuclear spins of close-by
46 H and Si atoms. While the g-tensor reflects the global electronic defect structure of the para-
47 magnetic defect, HFIs probe the defect wave function locally. Combining these two pieces
48 of information detailed spin-density⁹ maps of the unpaired electron spin may be obtained,
49 which constitute highly desired pieces of information to identify the microscopic origin of

50 the defect centers.

51 A detailed analysis of the EPR spectrum of coordination defects was first carried out by
52 Stutzmann *et al.* at a microwave frequency of 9 GHz (X-Band)¹. They determined the g-
53 tensor of the unpaired electron spin to be axially symmetric with principal values similar to
54 the P_b center occurring at the Si/SiO₂ interface^{10,11}. In a subsequent study, Umeda *et al.*¹²
55 revised the g-tensor values by studying the EPR spectrum at different resonance frequencies
56 (S-, X- and Q-band) with increased spectral resolution (see Table I). However, in both stud-
57 ies the g-tensor was already assumed as axially symmetric in the fitting models and never
58 systematically tested against rhombic symmetry. In addition to the g-tensor, Stutzmann *et*
59 *al.*¹ determined the HFI with the nuclear spin of the Si atom where most of the defect spin
60 density is concentrated. The HFI of this particular atom is characterized by an anisotropic
61 tensor, which will be denoted by \mathbf{A}_L in the following, i.e. the A-tensor with the largest
62 isotropic HFI. By analyzing the principal values of this tensor within an analytical linear
63 combination of atomic orbitals (LCAO) model¹³, Stutzmann *et al.*¹ determined the wave
64 function of the defect. Since their analysis of the HFI suggests that the defect wave func-
65 tion is sp^x-hybridized and of strong p-character, the authors concluded that the electronic
66 structure of the given center resembles a DB similar to the P_b center. However, the isotropic
67 HFI (A_{iso}) of coordination defects in a-Si:H, as evaluated by Stutzmann and Biegelsen^{1,14},
68 is given by $A_{\text{iso}} = 200$ MHz and is therefore much smaller than the isotropic HFI of the P_b
69 center ($A_{\text{iso}} = 315$ MHz)^{15,16}. This discrepancy was attributed to a relaxation of the atomic
70 structure of the DB from a tetrahedral configuration to a more planar geometry, induced by
71 the amorphous environment. It was argued that in the latter configuration the p-character
72 of the DB wave function is enhanced over the s-character, which leads to a smaller isotropic
73 HFI. It is, however, not *a priori* clear whether such a relaxation actually takes place when
74 a DB is created in a-Si:H. This question can only be clarified by a detailed quantitative
75 theoretical treatment of the atomic DB structure and the resulting EPR parameters, which
76 is still missing up to now.

77 The possibility to compare experimental g- and A-tensors in amorphous semiconductor ma-
78 terials with theoretical calculations came into reach only recently. This was mainly due to
79 two reasons. Firstly, precise g-tensor data is usually only available for crystalline materials
80 and secondly, a lack of *ab-initio* approaches capable of calculating g-tensors from complex
81 material structures. This situation changed with the advent of advanced density-functional

82 theory (DFT) methods, which proved to be able to reproduce experimentally determined
83 g -tensors even in complex Si materials^{17,18}. Up to now such studies have been restricted
84 to crystalline Si materials. One of the purposes of this study is to extend this powerful
85 approach to a-Si:H.

86 Here, we present a detailed experimental and theoretical analysis of the g -tensor and the
87 HFIs of the dominant defect center in a-Si:H. We employ high resolution EPR measurements
88 and complement them by DFT calculations capable of relating measured g - and A -tensors to
89 the spin-density distribution, binding geometry and electrostatic surrounding of the para-
90 magnetic site. The defects in a-Si:H are studied experimentally by multifrequency EPR
91 (S-band: 3.6 GHz/0.13 T, X-band: 9.7 GHz/0.34 T, Q-band: 34 GHz/1.2 T and W-band:
92 94 GHz/3.35 T). In the absence of field-dependent line broadening mechanisms and at high
93 signal to noise ratio (S/N), a high frequency spectrum is generally enough to determine
94 principal values of g - and A -tensors as well as their relative orientation. In the present case,
95 however, pronounced site-to-site variations of the principal g -values (g -strain) restrict the
96 determination of principal A -values at high resonance frequencies. This limitation can be
97 overcome by the multifrequency approach, which allows to separate field-independent (\mathbf{A})
98 and field-dependent (\mathbf{g}) spectral contributions. The HFIs are thereby best resolved at low
99 magnetic fields and corresponding frequencies (S-band and X-band), while principal values
100 of the g -tensor can be best determined at high frequencies (Q- and W-band). Furthermore,
101 we applied field-swept echo-detected (FSE) EPR instead of previously used continuous wave
102 (c.w.) EPR since FSE-EPR resolves broad, tailing spectral features better than c.w. EPR
103 techniques. g - and A -values are extracted from experimental FSE spectra by a robust it-
104 erative fitting procedure. As a result we show that the g -tensor symmetry of coordination
105 defects in a-Si:H is rhombic and therefore lower than axial symmetry as claimed in earlier
106 studies^{1,12}. This result is important to improve the reliability and precision of g -tensor values
107 and provides the basis for detailed studies of correlations between material properties and
108 \mathbf{g} ^{19,20}. Improved g -tensor values may also help to determine structural differences between
109 light-induced and native defects and thereby shed new light on physical processes underlying
110 the SWE.

111 In order to see whether or not the experimentally determined g - and A -values are adequately
112 described by the atomistic DB model, we employed 26 DB defect structures, generated in
113 two different ways by state of the art annealing techniques^{21,22}. Each model contained a

114 single DB defect. The g - and A -values of each DB model were then calculated by DFT
115 methods and compared to the experimentally obtained magnetic interaction parameters.

116 II. MATERIALS AND METHODS

117 Undoped a-Si:H samples were deposited with plasma-enhanced chemical vapor deposition
118 (PECVD) on a 10 cm \times 10 cm Mo foil at a substrate temperature of about 185 $^{\circ}$ C, of undi-
119 luted silane (silane concentration 100 %), pressure 0.7 mbar, power density of 130 mW/cm²,
120 interelectrode distance of 12 mm, resulting in a deposition rate of 1.8 nm/s. ESR powder
121 samples have been prepared as described in²³. The initial defect density of the samples as
122 determined by c.w. EPR is given by $N_D = 4(1) \cdot 10^{16}$ cm⁻³. The hydrogen content of the
123 sample is about 21 at. % as determined on a reference a-Si:H sample using Fourier-transform
124 infrared spectroscopy. The films were removed from the substrate by diluted hydrochloric
125 acid and flakes were collected in EPR-quartz tubes. Pulsed EPR spectroscopy at S-, X-
126 and Q-band was performed on a Bruker BioSpin ElexSys E580 spectrometer and EPR mea-
127 surements at W-band were performed on an ElexSys E680 spectrometer. The probe heads
128 employed at S-, X- and W-Band were a Bruker ER4118S-MS5, a Bruker ER4118X-MD5,
129 and a Bruker EN600-1021H, respectively. At Q-band a home-built probe head was used.
130 Temperature control was realized with CF935 helium bath cryostats and ITC503 tempera-
131 ture controllers from Oxford Instruments. All experiments were carried out at a temperature
132 of 80 K and utilized a typical field-swept echo (FSE) pulse sequence ($\pi/2 - \tau - \pi - \tau - \text{echo}$)
133 with a π pulse length of 40 ns, 32 ns, 80 ns, 128 ns and an interpulse delay τ of 400 ns, 300
134 ns, 400 ns, 300 ns at S-, X-, Q-, W-band, respectively. Spectra were independent of τ (data
135 not shown) and the shot-repetition time was set sufficiently long to avoid a saturation of the
136 spin system (> 2 ms). EPR spectra were accumulated about 1.5 h at Q- and W-band, and
137 about 10 h at S- and X-band due to lower sensitivity at these frequencies.

138 DFT calculations were carried out with a plane-wave pseudopotential formalism imple-
139 mented in the Quantum Espresso package²⁴. We used norm-conserving, scalar-relativistic
140 Troullier-Martins pseudopotentials and the PBE exchange-correlation functional. A plane-
141 wave energy cutoff of 30 Ry ensures convergence with respect to the basis set. The Brillouin
142 zone integration is done on a $6 \times 6 \times 6$ Monkhorst-Pack mesh. The HFIs of all atoms in the
143 supercell are determined from a projector augmented wave (PAW)-like post processing step

144 from the self-consistent calculation²⁵ using two projectors per 1-channel. Please note that
 145 the HFIs of ²⁹Si nuclear spins are mostly negative, since the nuclear g-value of ²⁹Si ($g_n =$
 146 -1.1106) is negative. The g-tensor is computed by the GI-PAW formalism¹⁷. We consider 26
 147 a-Si:H models consisting of 64 silicon and 8 hydrogen atoms. The defect-free a-Si:H models
 148 were created either by releasing hydrogen into Wooten-Winer-Weaire models of a-Si²¹, or
 149 by heating and gradually annealing of c-Si:H models followed by structural relaxation²².
 150 DBs were generated in these models by removing one of the hydrogen atoms, followed by
 151 structural relaxation.

152 III. RESULTS AND DISCUSSION

153 Fig. 1 depicts FSE spectra of a-Si:H powder samples taken at different microwave fre-
 154 quencies (S-, X-, Q- and W-band, respectively). In the left column (Fig. 1 a-d) experimental
 155 spectra taken at indicated frequency bands (crosses) are shown together with simulations
 156 obtained with parameters given in Table I (red solid lines). In the right column (Fig. 1 e-h)
 157 simulated FSE spectra in the absence of g-, A-strain and broadening due to unresolved HFIs
 158 are shown, to make the impact of \mathbf{g} and \mathbf{A} on the line shape at different resonance frequencies
 159 more obvious. In the following we will first qualitatively assign the frequency dependence of
 160 the EPR spectra to the dominating magnetic interactions. Secondly we describe the fitting
 161 routine applied to quantitatively extract the principal g- and A-values. Finally we com-
 162 pare these parameters with values derived from DFT calculations on computed a-Si:H DB
 163 models.

164 A. Analysis of multifrequency EPR spectra

165 The S- and X-band spectra (see Fig. 1 a,b) consist of an intense central line and two less
 166 intense satellite peaks (see enlarged spectral regions in Fig. 1a,b). Si enrichment studies
 167 showed that the EPR spectrum is subject to isotope effects, since naturally abundant Si
 168 is composed of stable non-magnetic isotopes (^{28/30}Si) with a total abundance of 95.32 %,
 169 and one stable magnetic isotope (²⁹Si) with an abundance of 4.68 %¹⁴. If the immediate
 170 vicinity of the defect is depleted from magnetic isotopes (²⁹Si and ¹H) large HFIs are ab-
 171 sent, resulting in the narrow central line, which is broadened by unresolved HFI to more

172 distant ^1H and ^{29}Si nuclei^{12,26}. This broadening of the resonance line is well described by
 173 a Lorentzian in the central part of the line (see Fig. 1a) and its width is proportional to
 174 the abundance of ^{29}Si , p , for $p < 10\%$ ¹². In cases, however, where Si atoms, which exhibit
 175 a significant spin density, are magnetic (^{29}Si isotope), the EPR spectrum is dominated by
 176 large HFIs (> 150 MHz, equivalent to > 7 mT) giving rise to satellite formation in the
 177 EPR spectrum. These satellites are symmetrically centered about the narrow central line
 178 (see Fig. 1 a and e). However, the satellites are already at S-band frequencies significantly
 179 broadened by site-to-site disorder resulting in a distribution of ^{29}Si HFIs (A-strain), which
 180 hampers the precise determination of ^{29}Si HFIs.

181 With increasing resonance frequency, the central line and the satellites exhibit increasing
 182 asymmetric line broadening, which may be attributed to g-anisotropy and g-strain. There-
 183 fore, the satellites, which are still resolved at X-band frequencies, overlap with the central
 184 line at Q- and W-band. Since the resolution of the principal g-values requires high frequen-
 185 cies, it becomes impossible to extract the magnetic parameters at one single frequency. It is
 186 important to note that a complete resolution of the principal g-values is not possible even
 187 at very high frequencies (see Fig. 1 d and h) since g-strain is proportional to the resonance
 188 frequency.

189 B. Modeling of multifrequency EPR spectra

190 The EPR spectrum may be described by the following spin Hamiltonian (\mathcal{H}) of a single
 191 electron spin ($S = 1/2$) coupled to n surrounding nuclei (indexed by j)²⁷:

$$\mathcal{H} = \mu_{\text{B}} \mathbf{B}_0 \mathbf{g} \mathbf{S} / \hbar + \sum_j \mu_{\text{N}} g_{jn} \mathbf{B}_0 \mathbf{I}_j / \hbar + \sum_j \mathbf{S} \mathbf{A}_j \mathbf{I}_j \quad (1)$$

192 where μ_{B} is the Bohr magneton and μ_{N} the nuclear magneton. The first term denotes
 193 the electron Zeeman interaction, which couples the electron spin S to the external magnetic
 194 field, \mathbf{B}_0 , via the anisotropic g-tensor, \mathbf{g} . The second term represents the nuclear Zeeman
 195 interaction of the coupled nuclear spins \mathbf{I}_j with \mathbf{B}_0 , where g_{jn} is the isotope dependent
 196 nuclear g-factor. The third term denotes the HFI, which describes the coupling of electron
 197 and nuclear spins by the A-tensor, \mathbf{A} . The A-tensor can be split into its isotropic part, \mathbf{A}_{iso}
 198 and its traceless, anisotropic part, $\mathbf{A}_{\text{aniso}}$. The isotropic part is given by the unit matrix times
 199 A_{iso} , which is proportional to the spin density at the nucleus (Fermi-contact interaction). In

200 case of axial symmetry, the anisotropic part can be expressed as

$$\mathbf{A}_{\text{aniso}} = \begin{pmatrix} -A_{\text{dip}} & & \\ & -A_{\text{dip}} & \\ & & 2A_{\text{dip}} \end{pmatrix}. \quad (2)$$

201 The g-tensor, \mathbf{g} , and the hyperfine tensor, \mathbf{A} , are 3x3 matrices with the principal values
 202 (g_x, g_y, g_z) and (A_x, A_y, A_z), respectively. Their respective principal axes systems are not
 203 necessarily collinear.

204 Due to the presence of strong g- and A-strain, the dominating A- and g-values cannot be
 205 extracted from the EPR spectra directly. Instead simultaneous simulations of the EPR spec-
 206 tra based on Eq. 1 have to be performed. If we assume that the spins are homogeneously
 207 distributed in the material (no clustering), only one electron spin needs to be included in the
 208 calculations since in that case the spin system is sufficiently dilute²⁷. The Zeeman term in
 209 Eq. 1 can then be solved exactly with the three principal values of the g-tensor as fit param-
 210 eters. The magnetic-field dependent broadening induced by g-strain is explicitly included in
 211 the simulation as an uncorrelated gaussian distribution of the principal values. This proce-
 212 dure has the advantage that the distribution parameters can be extracted directly from the
 213 fitting routine and are therefore separated from magnetic-field independent broadening. In
 214 contrast to the Zeeman term, the treatment of the HFI term in Eq. 1 is more complicated,
 215 because an exact simulation including all nuclei is impossible. We therefore introduce a
 216 fitting model with certain approximations. The HFI term in Eq. 1 is usually divided into
 217 two terms

$$\mathcal{H}_{\text{HFI}} = \sum_{k=1}^n \mathbf{S}\mathbf{A}_k\mathbf{I}_k + \sum_{j \neq k} \mathbf{S}\mathbf{A}_j\mathbf{I}_j \quad (3)$$

218 where the first term describes the resolved HFI, for which the EPR resonance positions are
 219 calculated explicitly in the simulation. The second term contains the unresolved HFIs which
 220 lead to a broadening of the magnetic resonance line. The line shape induced by unresolved
 221 HFIs is described by an empirical broadening function. This is a very convenient procedure,
 222 since the first term involves only a few nuclei, while the second term runs over a very large
 223 number of nuclei. The shape of the broadening function is usually well-described by one-
 224 or two-parameter functions like a Gaussian, Lorentzian or Voigtian²⁸⁻³⁰ which can be fitted
 225 to the resonance line by parameter adjustment. In addition to unresolved HFIs, paramag-

226 netic centers in the solid-state experience additional line broadening due to electron-electron
 227 spin-spin interaction and life-time broadening due to T_1 and T_2 mechanisms. However, for
 228 the low defect concentrations and the low temperatures used in this study both of these
 229 mechanisms contribute less than $1 \mu\text{T}$ to the line width and can therefore be neglected^{31,32}.
 230 This approximation is supported by the experimental observation that the line width of the
 231 broadening function is directly proportional to the ^{29}Si content of a-Si:H¹². We can therefore
 232 conclude that the broadening function is dominated by unresolved HFIs. It is important to
 233 note that due to the low natural abundance of ^{29}Si ($p = 4.68 \%$) the central line portion of
 234 the broadening function exhibits a Lorentzian and not a Gaussian shape^{12,30}.
 235 As in earlier studies we use a fitting model, where only one ^{29}Si nuclear spin is treated
 236 explicitly ($n = 1$ in Eq. 3, $\mathbf{A}_1 = \mathbf{A}_L$). The HFIs of all other spin carrying nuclei (such as ^1H ,
 237 ^{29}Si) are assumed to be unresolved and are taken into account by a Voigtian line broadening
 238 function^{1,12}. In addition, we limit the number of fitting parameters by introducing several
 239 prior assumptions for the symmetry of the \mathbf{A}_L -tensor and the orientation between the g-
 240 and \mathbf{A}_L -tensor. Since the satellites are strongly affected by inhomogeneous broadening it is
 241 difficult to test the symmetry of the \mathbf{A}_L -tensor against rhombicity. Furthermore, the rel-
 242 ative orientation between the \mathbf{A}_L - and g-tensor and its distribution cannot be determined
 243 independently, so we simply assume that both tensors are collinear with g_z and A_z being
 244 parallel. The principal values of \mathbf{A}_L are distributed (A-strain) and we included this effect in
 245 the simulation as an uncorrelated gaussian distribution of the principal values. It is assumed
 246 that the principal values of \mathbf{A}_L are not correlated to the principal values of \mathbf{g} (uncorrelated
 247 g- and A-strain).

248 C. Multifrequency fitting algorithm

249 To extract the A- and g-values we applied the following step-wise fitting routine. In a
 250 first step, the Q- and W-band spectra were fitted simultaneously by adjusting the distribu-
 251 tion parameters of the three principal g-values (mean value and standard deviation). In a
 252 second step, the S- and X-band spectra were fitted by adjusting the distribution parameters
 253 of the \mathbf{A}_L -tensor principal values, where we again assumed independent normal distribu-
 254 tions. In a third step, the S-band spectrum was fitted by adjusting a convolutional Voigtian
 255 line broadening function accounting for inhomogeneous broadening by unresolved HFI. The

256 three steps were repeated in a loop until convergence is reached. The simulations of the
 257 individual solid-state EPR spectra were performed with EasySpin, a MATLAB (The Math-
 258 works, Natick, MA, USA) toolbox³³. Powder EPR spectra are evaluated by considering a
 259 large set of different orientations uniformly distributed over the unit sphere. The simulated
 260 spectra are fitted to the experimental spectra by nonlinear least-squares methods using a
 261 trust-region-reflective algorithm implemented in MATLAB^{34,35}. Standard errors of fit pa-
 262 rameters indicating a significance level of 1σ are calculated by a linear sum of statistical
 263 and systematic errors. Statistical errors due to spectral noise are estimated by calculating
 264 asymptotic confidence intervals in a fixed-regressor model (for details see Ref.³⁶, chapter 5).
 265 Systematic errors arise due to imprecise measurement of the regressors (magnetic field and
 266 microwave frequency). While measurement errors of the microwave frequency are usually
 267 < 1 kHz and therefore negligible, the magnetic field at the sample position is not measured
 268 directly, but has to be calibrated with a field standard sample (LiLiF, BDPA). Typical errors
 269 of such calibrations and drifts of the magnetic field over time are 0.1 mT at high magnetic
 270 fields (Q- and W-band) and 0.02 mT at low magnetic fields (S- and X-band). We roughly
 271 estimated the impact of these measurement errors on the fit parameters by repeating the
 272 above multifrequency fit routine for a worst case scenario, where all magnetic-field axes are
 273 offset by the estimated measurement error. The obtained errors of the fit parameters are
 274 then assigned to a standard error (significance level 1σ) to indicate the uncertainty of the
 275 fit parameter values.

276 **D. Multifrequency fit results**

277 The fit results for a rhombic g-tensor are shown as solid lines in Fig. 1 a-d. In ear-
 278 lier publications it was explicitly assumed that the g-tensor is axially symmetric, i.e.
 279 $g_x = g_y = g_{\perp}$ and $g_z = g_{\parallel}$. In order to test this hypothesis, we performed two separate mul-
 280 tifrequency fits. In a first fit the symmetry of the g-tensor is forced to axial symmetry and
 281 in a second fit (see Fig. 1 a-d) no assumptions about the symmetry were made. In the first
 282 case the principal values of the g-tensor are $g_x = g_y = 2.0065(2)$ and $g_z = 2.0042(2)$, in very
 283 good agreement with earlier studies (see Ref.¹² and Table I). In the second case we obtained
 284 a rhombic g-tensor with three different principal values ($g_x = 2.0079(2)$, $g_y = 2.0061(2)$ and
 285 $g_z = 2.0034(2)$). However, the quality of the fit, measured by the sum of squares of the fit

286 residuals $\|r\|_2^2$ (difference between the fitted and the experimental spectra), is significantly
 287 worse in the case of an axially symmetric g-tensor as compared to a rhombic g-tensor (see
 288 Table I). On the basis of our fit results, we can state that g_x and g_y do not coincide on a
 289 significance level of $\approx 5\sigma$. We therefore conclude that coordination defects in a-Si:H exhibit
 290 a rhombic g-tensor.

291

292 For the A_L -tensor we obtained $A_x = A_y = 151(13)$ MHz and $A_z = 269(21)$ MHz, which
 293 corresponds to $A_{\text{iso}} = 190(11)$ MHz and $A_{\text{dip}} = 39(8)$ MHz. Please note that we only
 294 report magnitude values for the HFIs since FSE-EPR does not provide the sign of the
 295 HFIs. These values are slightly smaller than the previously reported ones (see Table I). The
 296 Voigtian broadening function, accounting for unresolved HFI, deviates only slightly from a
 297 pure Lorentzian function since the FWHM of the Gaussian component is about a factor of
 298 4 smaller than the FWHM of the Lorentzian component (see Table I). A complete overview
 299 of the various fit parameter sets including literature values is given in Table I.

300 E. DFT calculations of DB g- and A-tensors

301 The above analysis of the experimental spectra provided g- and A-values of paramagnetic
 302 coordination defects present in a-Si:H. Our task is now to deduce the microscopic origin of
 303 the defect centers from the obtained interaction values. In order to test the hypothesis that
 304 coordination defects in a-Si:H are DB defects we examined g- and A-values of computer-
 305 generated DB defect models by DFT calculations. As outlined above, DB defects were
 306 created in a-Si:H computer models by removing a single H atom from defect-free structures.
 307 However, it is important to note that theoretical modeling of DB defects in a-Si:H is a
 308 demanding task since the atomic defect structure is not well defined as in case of P_b defects
 309 at the Si/SiO₂ interface. Disorder in amorphous materials induces a large variety of atomic
 310 configurations. In order to account for this variety we modeled a large number of different
 311 defect structures (26 in total) and calculated the resulting g- and A-values. The aim of
 312 this approach is to link the observed g- and A-values with particular features of the atomic
 313 structure. However, to our surprise we found that quite different spin-density distributions
 314 result in very similar g-values.

315 To illustrate this finding we compare calculated ground-state spin-densities, g- and A_L -

316 tensors of two particular computer-generated DB models. The first DB model (DB1) is
 317 displayed in Fig. 2a ($g_x = 2.0091$, $g_y = 2.0057$, $g_z = 2.0024$, and $A_x = -291$ MHz, $A_y = -288$
 318 MHz, $A_z = -427$ MHz for the ^{29}Si \mathbf{A}_L -tensor) and the second DB model (DB2) is shown
 319 in Fig. 2b ($g_x = 2.0095$, $g_y = 2.0065$, $g_z = 2.0034$, and $A_x = -176$ MHz, $A_y = -180$ MHz,
 320 $A_z = -236$ MHz for the ^{29}Si \mathbf{A}_L -tensor). The g-tensor symmetry of both models is clearly
 321 rhombic, while the \mathbf{A}_L -tensor is very close to axial symmetry. Already from a superficial
 322 inspection of the two structures it becomes apparent that the wave function of DB1 is mainly
 323 localized on a single Si atom, while the wave function of DB2 is more delocalized. Despite
 324 the apparent discrepancy of the spin-density distributions, the g-tensor principal values of
 325 both models are almost identical. Hence, widely different configurations can yield almost
 326 identical g-tensors. This effect will be discussed in more detail below. In contrast to the
 327 almost identical g-tensor, the HFI and the relative orientation between g- and \mathbf{A}_L -tensor
 328 vary drastically. The isotropic HFI of DB2 ($A_{\text{iso}} = -197$ MHz) is much smaller than the
 329 isotropic HFI of DB1 ($A_{\text{iso}} = -335$ MHz), which can be attributed to a delocalization of the
 330 DB wave function. The axes of the g_z and A_z principal values are nearly parallel in case of
 331 DB1 but differ significantly in case of DB2 (see Fig. 2a,b).

332 F. Comparison of experimental and theoretical results

333 We have observed that the two computer-generated defect structures analyzed above
 334 show a substantial variation in terms of spin-density distribution. This variation is a result
 335 of site-to-site disorder present in a-Si:H leading to a wide distribution of A- and g-values
 336 (A- and g-strain). It is therefore clear that a comparison of g- and A-values from only one
 337 or two computer models is not sufficient for a successful identification of the microscopic
 338 origin of defect centers in a-Si:H. Instead, it is mandatory to evaluate a representative
 339 number of DB models and their electronic structure to cover the whole spread of g- and
 340 A-value distributions. We therefore extend our analysis to a larger set of defect models,
 341 which includes 26 DB models in total. Histograms of g- and A-values of those models are
 342 shown in Fig. 3 and 4 and compared to experimental distribution functions obtained by the
 343 multifrequency fit. A compilation of principal values of \mathbf{g} and \mathbf{A}_L and plots of spin-density
 344 distributions for each DB model can be found in the supplemental material³⁷. An inspection
 345 of the spin-density distribution of individual DB defects shows that the majority of defects

346 exhibits a spin-density distribution which is bound to a single, undercoordinated, Si atom.
347 In the following we will compare the g- and A-tensors obtained from DFT with the respective
348 parameters extracted from multifrequency EPR data.

349 1. *g*-tensor

350 In Fig. 3 the distribution of principal values of \mathbf{g} derived from computer models are
351 plotted together with experimental distribution functions. The distribution mean values and
352 width of theoretically obtained values and their uncertainties can be estimated by fitting a
353 normal distribution to the g-values. The mean of the calculated values are $g_x = 2.0093(7)$,
354 $g_y = 2.0064(5)$ and $g_z = 2.0035(3)$. Comparing those values to the experimental results
355 ($g_x = 2.0079(2)$, $g_y = 2.0061(2)$ and $g_z = 2.0034(2)$) shows that the experimental g_y and g_z
356 principal values deviate less than one σ from the theoretical values, while g_x deviates about
357 two σ (see also error bars in Fig. 3). This analysis shows that there is a good agreement
358 for the g_y and g_z mean principal values, while there is a significant deviation in the case of
359 g_x . In all three cases the spread of the computed principal g-values significantly exceeds the
360 spread of the experimental distributions (see Fig. 3 and Table I).

361 By inspecting distributions of g_x , g_y and g_z separately, we see that they peak at different
362 values, although parts of the distributions overlap. By analyzing Fig. 3, it becomes clear that
363 the g_z distribution peaks close to the free-electron g-value ($g_e = 2.0023$) and is well separated
364 from the g_x and g_y distribution. However, since there is a large overlap between distributions
365 of g_x and g_y , it is not immediately clear whether the distributions are independent or if g_x and
366 g_y actually belong to the same distribution as it would be the case for an axially symmetric
367 g-tensor. In that case the distribution would be much wider, but still most of the g-tensors
368 would exhibit a slight rhombic symmetry. It is therefore necessary to determine the g-tensor
369 rhombicity of each DB model separately by calculating $(g_x - g_y)/(g_x - g_z)$. By doing so
370 we found that each individual g-tensor is clearly rhombic and the distribution peaks at 0.5
371 which fits well to the experimentally obtained symmetry.

372 It appears to be surprising that g-tensors of DB defects with a very symmetric spin-density
373 distribution (see Fig. 2a) exhibit rhombic symmetry and not axial symmetry. This effect
374 can be rationalized as follows. The anisotropy of the g-tensor and isotropic shifts from g_e
375 result from an indirect coupling of the electron spin to the external magnetic field mediated

376 by the orbital momentum. In the picture of second order perturbation theory³⁸, the most
 377 important contribution arises from the interplay of the singly-occupied DB orbital ψ_p with
 378 all unoccupied or occupied orbitals ψ_n other than ψ_p (orbital energies ϵ_n and ϵ_p) weighted
 379 by their inverse energetic separation,

$$g_{\alpha\beta} = \delta_{\alpha\beta}g_e + \dots + 2 \sum_{n \neq p} \frac{\langle \psi_p | \lambda L_\alpha | \psi_n \rangle \langle \psi_n | L_\beta | \psi_p \rangle}{\epsilon_p - \epsilon_n} \quad (4)$$

380 Here, \mathbf{L} denotes the angular momentum operator and λ the spin-orbit coupling constant.
 381 Even in case of a DB orbital, which is completely localized at the threefold-coordinated Si
 382 atom, the g-tensor is obviously sensitive to changes in the orientation and energies of the
 383 other orbitals. To simplify the discussion of the g-tensor anisotropy, let us assume that the
 384 singly-occupied DB orbital ψ_p is given by a pure $|p_z\rangle$ orbital and the other orbitals $|p_{x,y}\rangle$ are
 385 also of atomic type. We define the Cartesian coordinate system such that the z-axis coincides
 386 with the axis of the DB orbital. By this we can show that the paramagnetic contribution
 387 vanishes for $\alpha\beta = zz$, since $L_z |p_z\rangle = 0$. Significant deviations from g_e are therefore only
 388 expected for $g_x \equiv g_{xx}$ and $g_y \equiv g_{yy}$ given by

$$\begin{aligned} \Delta g_{xx} &= 2 \frac{\langle p_z | \lambda L_x | p_y \rangle \langle p_y | L_x | p_z \rangle}{\epsilon_{p_z} - \epsilon_{p_y}} = 2 \frac{\lambda}{\epsilon_{p_z} - \epsilon_{p_y}}, \\ \Delta g_{yy} &= 2 \frac{\langle p_z | \lambda L_y | p_x \rangle \langle p_x | L_y | p_z \rangle}{\epsilon_{p_z} - \epsilon_{p_x}} = 2 \frac{\lambda}{\epsilon_{p_z} - \epsilon_{p_x}}. \end{aligned} \quad (5)$$

389 We see that if the degeneracy of the p_x and p_y orbitals is lifted, the g_{xx} and g_{yy} values
 390 will not be degenerate. In a most disordered environment like a-Si:H one expects that the
 391 degeneracy is lifted due to fluctuations of the bond-angles and bond-length. As a result a
 392 rhombic g-tensor instead of an axially symmetric one arises. This analysis is also valid for
 393 the more realistic case of $\psi_{p,n}$ being molecular orbitals.

394 We have seen that there is a quantitatively good agreement of the calculated g-tensors of
 395 DB models and the experimentally determined g-tensor of coordination defects in a-Si:H.
 396 However, we have shown that the g-tensor principal values are rather insensitive to the spin-
 397 density distribution of DBs. Widely different wave functions give rise to almost identical
 398 g-tensors. We now extend our analysis to the principal values of \mathbf{A}_L , which are a more
 399 precise probe of the local spin-density distribution of the defect center.

401 The histogram in Fig. 4a shows a comparison of principal \mathbf{A}_L -values derived from dif-
 402 ferent computer-generated DB models with experimentally obtained values. Theoretically
 403 obtained distributions were approximated by normal distributions. It is found that val-
 404 ues derived from computer-generated DBs deviate from values determined by the multifre-
 405 quency fit. The absolute mean of all three principal values of \mathbf{A}_L obtained by theory are
 406 $A_x = 213(14)$ MHz, $A_y = 216(14)$ MHz and $A_z = 327(17)$ MHz, whereas the experimental
 407 values are $A_x = 151(13)$ MHz, $A_y = 151(13)$ MHz and $A_z = 269(21)$ MHz. The theoretical
 408 HFI values are therefore larger than the experimental values by at least 2σ (see also error
 409 bars in Fig. 4a)). The discrepancy of \mathbf{A}_L between experiment and theory is therefore much
 410 more pronounced than in the case of \mathbf{g} . As observed for the \mathbf{g} -tensor, the calculations lead
 411 to a larger distribution of principal values as compared to experiment.

412 A_x and A_y distributions in computer models are clearly degenerate and strongly differ from
 413 A_z . This hints towards an A-tensor close to axial symmetry. To check whether the A_x and
 414 A_y distributions of the computer models are independent or not, we determined the rhom-
 415 bicity $(A_x - A_y)/(A_x - A_z)$ of each set of principal values and found that the \mathbf{A}_L -tensors
 416 for all models investigated are indeed very close to axial symmetry. These results support
 417 the previously made assumption of an axially symmetric \mathbf{A}_L -tensor for the fits of the EPR
 418 spectra in Fig. 1.

419 The calculations revealed a rather peculiar deviation of the symmetry properties of \mathbf{g} and
 420 \mathbf{A}_L , where \mathbf{g} exhibits rhombic symmetry and \mathbf{A}_L axial symmetry. The apparent discrepancy
 421 in the symmetry properties can be rationalized as follows. The \mathbf{A}_L -tensor depends directly
 422 on the ground-state spin density and is strongly dominated by the local-orbital character
 423 (sp^x hybrid) of the DB state at the site of the trivalent Si atom. Structural variations due to
 424 the amorphous matrix affect its orientation and possibly the degree of s-p hybridization, but
 425 do not alter the fundamental sp^x character of the DB orbital. Its axial symmetry properties
 426 are therefore maintained even in the presence of large disorder-induced fluctuations of the
 427 bond-length and bond-angles in a-Si:H. This does also hold in good approximation for the
 428 HFIs of ^{29}Si atoms in the first and second coordination shell.

429 We have seen that some of our defect models exhibit a significant spin delocalization. Yet,
 430 all defect models exhibit typical DB characteristics of a spin density mainly localized on a

431 single, undercoordinated atom (referred to as the central atom), while the spin density on
 432 the other atoms is significantly smaller. This is reflected by the fact that Si atoms with the
 433 second-largest HFI have values that average to $A_{\text{iso}} = -79(5)$ MHz and $A_{\text{dip}} = -7(4)$ MHz
 434 (see Fig. 4b).

435 We have seen that the mean principal values of \mathbf{A}_L deviate between theory and experiment.
 436 Decomposing \mathbf{A}_L into an isotropic and anisotropic part clearly shows that this discrepancy
 437 arises from the isotropic part (A_{iso}) while the anisotropic HFI (A_{dip}) in both cases equals
 438 about 35 to 40 MHz (see Table I). The most puzzling fact comparing computed and exper-
 439 imentally obtained HFIs is therefore the discrepancy of the mean isotropic HFI with the
 440 following values for theory and experiment:

$$\text{theory} : |A_{\text{iso}}| = 252(9) \text{ MHz} \quad (6)$$

$$\text{experiment} : |A_{\text{iso}}| = 190(11) \text{ MHz}. \quad (7)$$

441 These values reveal two important findings. Firstly the experimentally obtained A_{iso} of
 442 coordination defects in a-Si:H is smaller than the value derived from the DFT calculations
 443 with a level of confidence of more than 2σ . Secondly, both values are much smaller than
 444 A_{iso} of P_b centers at the Si/SiO₂ interface (315 MHz)^{15,16}, which was frequently employed as
 445 model system for the coordination defects in a-Si:H. The first finding may be rationalized by
 446 an inspection of the computer-generated spin density maps. We find that the lower value of
 447 A_{iso} in a-Si:H as compared to P_b centers is primarily caused by a delocalization of the DB spin
 448 density. In contrast to previous assumptions, we did not find any evidence for a relaxation
 449 of the atomic structure which could lead to a reduction of A_{iso} ¹. Our results render the
 450 relaxation of DBs in a-Si:H towards a more planar defect geometry improbable. Hence, the
 451 observed deviation between experimental and theoretical values of A_{iso} , our second finding,
 452 must be of different origin. One possible explanation is that the chosen population of defect
 453 structures in the DFT calculation may not represent the paramagnetic site in a-Si:H. This
 454 again raises a heavily debated question: Which kind of coordination defect gives rise to the
 455 EPR signal centered around $g = 2.0055$? Due to the limited number of model structures
 456 in this work, it cannot be excluded that coordination defects in a-Si:H form DB structures,
 457 which are not contained in the DFT defect pool or that the microscopic structure of the
 458 defects completely differs from a DB. If coordination defects exhibit more delocalized spin

459 densities than random DBs considered in this work, the largest isotropic HFI will be smaller.
460 A more delocalized defect structure is therefore one possibility to explain the discrepancy
461 between experiment and model calculations.

462 In view of these results, it is evident that the structural models employed for the theoretical
463 analysis miss an important aspect of the experimentally observed defect ensemble. An
464 obvious weakness of the theoretical modeling is that the DBs were created at random points
465 in the amorphous network and were subject only to local relaxation. More complex, but
466 slow (> 10 ns) relaxation mechanisms possibly occurring in the real material are therefore
467 not captured at all. If present, such relaxations might select a subset of the present defect
468 models, or even other configurations. For instance, the floating-bond type defect exhibits
469 states delocalized over several Si atoms^{39,40}. However, the floating-bond model has long been
470 rejected, being in conflict with a number of other experimental observations³⁹⁻⁴². At present
471 we can only speculate over plausible microscopic defect models since the available data do
472 not allow us to discriminate them.

473 IV. CONCLUSIONS

474 Using a multifrequency approach, we have determined g-tensor principal values of co-
475 ordination defects in a-Si:H: $g_x = 2.0079$, $g_y = 2.0061$ and $g_z = 2.0034$ with improved
476 accuracy (see Table I). In contrast to earlier studies^{1,12}, we found that the g-tensor shows
477 pronounced rhombicity. In addition, we carried out a first systematic study where exper-
478 imental g- and A_L -values (²⁹Si-HFI tensor with the largest isotropic part) are compared
479 to theoretical values obtained by DFT calculations of 26 different a-Si:H DB models. As
480 main conclusions we found that computer models reproduce the experimentally observed
481 principal values and rhombicity of the g-tensor, but do not exhibit HFIs in agreement with
482 experiment. The apparent discrepancy between symmetry properties of g- and A-tensors is
483 attributed to the fact that the g-tensor reflects the global electronic defect structure while
484 the A-tensor is exclusively determined by the local spin-density distribution in the vicinity
485 of the nucleus of interest. This leads to a situation where DBs with a localized and a delo-
486 calized spin-density distribution exhibit almost identical g-tensors. Principal values of the
487 A_L -tensor for computer generated DB models disagree with experimental values obtained
488 by the multifrequency fit. The isotropic HFI of the DB models is on average $A_{\text{iso}} = -252$

489 MHz which is much larger than the fit result, $A_{\text{iso}} = 190$ MHz. Our DFT calculations do
490 not support the hypothesis formulated in earlier studies that the structure of DB defects
491 relaxes towards a more planar geometry and thereby reduces the isotropic HFI. These ob-
492 servations strongly suggest that coordination defects in a-Si:H are more delocalized than
493 investigated DB computer models. We therefore conclude that coordination defects in a-
494 Si:H are not well-described within the random DB model. However, to develop plausible
495 alternative models, additional DFT studies are required. Such studies are on the way within
496 the research network *EPR-Solar*.

497 ACKNOWLEDGMENTS

498 Financial support from BMBF (EPR-Solar network project 03SF0328) is acknowledged.
499 We are very grateful to F. Inam (ICTP, Italy) and D. Drabold (Ohio University, USA) as
500 well as K. Jarolimek (TU Delft, Netherlands) for providing us the DB model structures
501 used in the theoretical calculations. U. Gerstmann (University of Paderborn, Germany), M.
502 Stutzmann and M. Brandt (TU Munich, Germany) are gratefully acknowledged for helpful
503 discussions.

504 * matthias.fehr@helmholtz-berlin.de

505 † christian.teutloff@fu-berlin.de

506 ¹ M. Stutzmann and D. K. Biegelsen, Phys. Rev. B **40**, 9834 (1989).

507 ² M. Stutzmann, Philos. Mag. B **60**, 531 (1989).

508 ³ H. Dersch, J. Stuke, and J. Beichler, Appl. Phys. Lett. **38**, 456 (1981).

509 ⁴ D. L. Staebler and C. R. Wronski, Appl. Phys. Lett. **31**, 292 (1977).

510 ⁵ D. L. Staebler and C. R. Wronski, J. Appl. Phys. **51**, 3262 (1980).

511 ⁶ H. Fritzsche, Annu. Rev. Mater. Res. **31**, 47 (2001).

512 ⁷ M. Zeman, G. Van Elzakker, F. D. Tichelaar, and P. Sutta, Philos. Mag. **89**, 2435 (2009).

513 ⁸ M. Fehr, A. Schnegg, B. Rech, K. Lips, F. Finger, O. Astakhov, C. Teutloff, and R. Bittl, phys.
514 stat. sol. (a) **207**, 552 (2010).

515 ⁹ Throughout the text the term spin density denotes the spin distribution over the atomic orbitals,
516 whereas defect density denominates the concentration of paramagnetic defects in the material.

517 ¹⁰ E. H. Poindexter, P. J. Caplan, B. E. Deal, and R. R. Razouk, *J. Appl. Phys.* **52**, 879 (1981).

518 ¹¹ M. Cook and C. T. White, *Phys. Rev. B* **38**, 9674 (1988).

519 ¹² T. Umeda, S. Yamasaki, J. Isoya, and K. Tanaka, *Phys. Rev. B* **59**, 4849 (1999).

520 ¹³ G. D. Watkins and J. W. Corbett, *Phys. Rev.* **134**, A1359 (1964).

521 ¹⁴ D. K. Biegelsen and M. Stutzmann, *Phys. Rev. B* **33**, 3006 (1986).

522 ¹⁵ K. L. Brower, *Appl. Phys. Lett.* **43**, 1111 (1983).

523 ¹⁶ W. E. Carlos, *Appl. Phys. Lett.* **50**, 1450 (1987).

524 ¹⁷ C. J. Pickard and F. Mauri, *Phys. Rev. Lett.* **88**, 086403 (2002).

525 ¹⁸ U. Gerstmann, M. Rohrmüller, F. Mauri, and W. G. Schmidt, *phys. stat. sol. (c)* **7**, 157 (2010).

526 ¹⁹ O. Astakhov, R. Carius, F. Finger, Y. Petrusenko, V. Borysenko, and D. Barankov, *Phys. Rev.*
527 *B* **79**, 104205 (2009).

528 ²⁰ Y. Wu and A. Stesmans, *Phys. Rev. B* **38**, 2779 (1988).

529 ²¹ P. Biswas, D. N. Tafen, F. Inam, B. Cai, and D. A. Drabold, *J. Phys.: Condens. Matter* **21**,
530 084207 (2009).

531 ²² K. Jarolimek, R. A. de Groot, G. A. de Wijs, and M. Zeman, *Phys. Rev. B* **79**, 155206 (2009).

532 ²³ L. Xiao, O. Astakhov, and F. Finger, *Jpn. J. Appl. Phys.* **50** (2011).

533 ²⁴ P. Giannozzi, S. Baroni, N. Bonini, M. Calandra, R. Car, C. Cavazzoni, D. Ceresoli, G. L.
534 Chiarotti, M. Cococcioni, I. Dabo, A. Dal Corso, S. De Gironcoli, S. Fabris, G. Fratesi,
535 R. Gebauer, U. Gerstmann, C. Gougoussis, A. Kokalj, M. Lazzeri, L. Martin-Samos, N. Marzari,
536 F. Mauri, R. Mazzarello, S. Paolini, A. Pasquarello, L. Paulatto, C. Sbraccia, S. Scandolo,
537 G. Sciauzero, A. P. Seitsonen, A. Smogunov, P. Umari, and R. M. Wentzcovitch, *J. Phys.:*
538 *Condens. Matter* **21**, 395502 (2009).

539 ²⁵ C. G. Van De Walle and P. E. Blöchl, *Phys. Rev. B* **47**, 4244 (1993).

540 ²⁶ M. S. Brandt, M. W. Bayerl, M. Stutzmann, and C. F. O. Graeff, *J. Non-Cryst. Solids* **227-230**,
541 343 (1998).

542 ²⁷ N. M. Atherton, *Principles of electron spin resonance* (Ellis Horwood: PTR Prentice Hall, New
543 York, 1993).

544 ²⁸ J. A. Weil, *Mol. Phys. Rep.* **26**, 11 (1999).

545 ²⁹ J. H. Van Vleck, *Phys. Rev.* **74**, 1168 (1948).

- 546 ³⁰ C. Kittel and E. Abrahams, Phys. Rev. **90**, 238 (1953).
- 547 ³¹ S. J. Wyard, Proc. Phys. Soc. London **86**, 587 (1965).
- 548 ³² M. Stutzmann and D. K. Biegelsen, Phys. Rev. B **28**, 6256 (1983).
- 549 ³³ S. Stoll and A. Schweiger, J. Magn. Res. **178**, 42 (2006).
- 550 ³⁴ T. F. Coleman and Y. Li, Siam J. Optim. **6**, 418 (1996).
- 551 ³⁵ T. F. Coleman and Y. Li, Math. Program. **67**, 189 (1994).
- 552 ³⁶ G. A. F. Seber and C. J. Wild, *Nonlinear regression* (Wiley, New York, 1989).
- 553 ³⁷ See EPAPS Document No. [number will be inserted by publisher] for details on DFT calculations
554 of computer-generated DB models.
- 555 ³⁸ A. J. Stone, Proc. R. Soc. London, Ser. A **271**, 424 (1963).
- 556 ³⁹ P. A. Fedders and A. E. Carlsson, Phys. Rev. B **37**, 8506 (1988).
- 557 ⁴⁰ R. Biswas, C. Z. Wang, C. T. Chan, K. M. Ho, and C. M. Soukoulis, Phys. Rev. Lett. **63**, 1491
558 (1989).
- 559 ⁴¹ P. A. Fedders and A. E. Carlsson, Phys. Rev. B **39**, 1134 (1989).
- 560 ⁴² N. Ishii and T. Shimizu, Phys. Rev. B **42**, 9697 (1990).

TABLE I. Summary of experimental (multifrequency fit) and theoretical g-tensor and A_L -tensor principal values for coordination defects in a-Si:H. Full-width half maximum (FWHM) of gaussian distributions of the g- and A_L -tensor principal values (g- and A-strain) are given in square brackets. The Voigt function accounting for magnetic-field independent broadening is characterized by FWHM of Gaussian and Lorentzian components denoted by $\Delta B^{G/L}$. Standard errors of the fit parameters (significance level 1σ) are calculated by a linear sum of statistical and systematic errors (for details see text) and are given in round brackets. $\|r\|_2^2$ denotes the sum of squares of the fit residual r in units of the sum of squares of the experimental data.

	principal values of g-tensor			principal values of ^{29}Si A_L -tensor				broadening function	$\ r\ _2^2$ in %
	g_x or g_\perp [strain] ^a	g_y or g_\perp [strain] ^a	g_z or g_\parallel [strain] ^a	A_x or A_\perp in MHz ^b	A_y or A_\perp in MHz ^b	A_z or A_\parallel in MHz ^b	$A_{\text{iso}}/A_{\text{dip}}$ in MHz ^b	Voigtian $\Delta B^{G/L}$ in mT	
(EPR)									
Present ^c	2.0079(2) [0.0054(1)]	2.0061(2) [0.0022(1)]	2.0034(2) [0.0018(1)]	151(13) [46(27)]	151(13) [46(27)]	269(21) [118(66)]	190(11)/39(8)	0.13(3)/0.43(1)	0.2
Present ^d	2.0065(2) [0.0047(1)]	2.0065(2) [0.0047(1)]	2.0042(2) [0.0019(1)]	149(15) [47(32)]	149(15) [47(32)]	265(26) [113(75)]	188(13)/39(10)	0.15(3)/0.42(1)	0.3
Ref. ¹²	2.0065 [N/A] ^e	2.0065 [N/A] ^e	2.0039 [N/A] ^e	143 [56]	143 [56]	333 [73]	206/63	N/A ^e	
Ref. ¹	2.0080 [0.0029]	2.0080 [0.0029]	2.0040 [0.0022]	154 [28]	154 [28]	305 [56]	205/50	not specified	
(Theory)									
Present ^f	2.0093(7) [0.0084(12)]	2.0064(5) [0.0060(9)]	2.0035(3) [0.0035(5)]	-213(14) [166(24)]	-216(14) [166(24)]	-327(17) [203(30)]	-252(9)/-37(7)	non-analytic ^g	

^a ΔB value given in mT converted to Δg (dimensionless) using $\Delta g = (g_e^2 \mu_B / h) \cdot (\Delta B / \nu)$

^b Hyperfine interactions given in mT converted to MHz using $\nu_{\text{HFI}} = g_e \mu_B B / h$

^c Multifrequency fit without prior assumptions about the symmetry of \mathbf{g}

^d Multifrequency fit assuming axial symmetry of \mathbf{g}

^e g-strain and magnetic-field independent broadening are entangled in the analysis of Ref.¹² and could not be separated.

^f DFT calculation of DB defect center in a relaxed a-Si₆₄H₇ supercell

^g The broadening function of the DFT data cannot be expressed in closed analytic form.

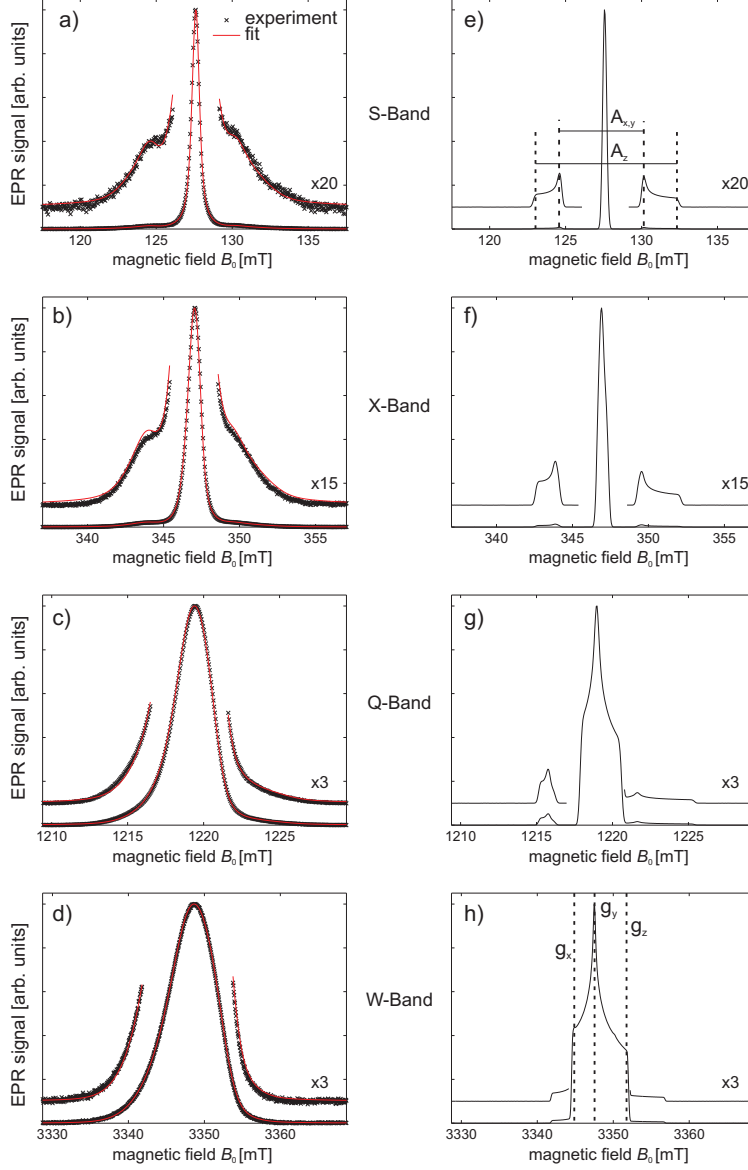


FIG. 1. S-/X-/Q- and W-band field-swept echo EPR spectra of defects in a-Si:H ($g = 2.0055$) at a temperature of 80 K. Each spectrum was recorded by integrating the primary echo of a $(\pi/2 - \tau - \pi - \tau - \text{echo})$ pulse sequence. Left column (a-d): experimental spectra (crosses) and the fitted spectra (red solid line) obtained with the model described in the text. Spectra are offset vertically for clarity. Right column (e-h): fitted spectra without g-strain, A-strain and isotropic magnetic field broadening. Principal values of the g-tensor and the A_L -tensor are indicated by the vertical and horizontal lines in e) and h).

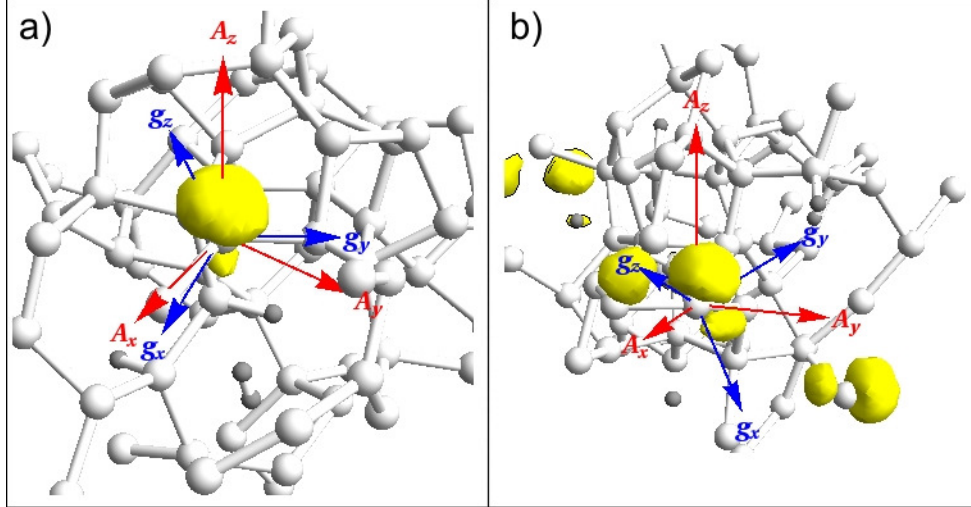


FIG. 2. Two selected computer-generated atomistic models of a DB in a-Si:H (for details see text). Principal values of \mathbf{g} and \mathbf{A}_L for the two models are a) $g_x = 2.0091$, $g_y = 2.0057$, $g_z = 2.0024$, and $A_x = -291$ MHz, $A_y = -288$ MHz, $A_z = -427$ MHz, b) $g_x = 2.0095$, $g_y = 2.0065$, $g_z = 2.0034$, and $A_x = -176$ MHz, $A_y = -180$ MHz, $A_z = -236$ MHz. Atoms are indicated by light-gray (Si) and dark-gray (H) shaded spheres. Isosurface plot of the electron spin density (isosurface at 10 % of maximum spin-density value) of the trivalent silicon atom is show in yellow. Eigenvectors of the g-tensor are indicated by blue arrows and the eigenvectors of the \mathbf{A}_L -tensor of the threefold-coordinated Si atom are indicated by red arrows.

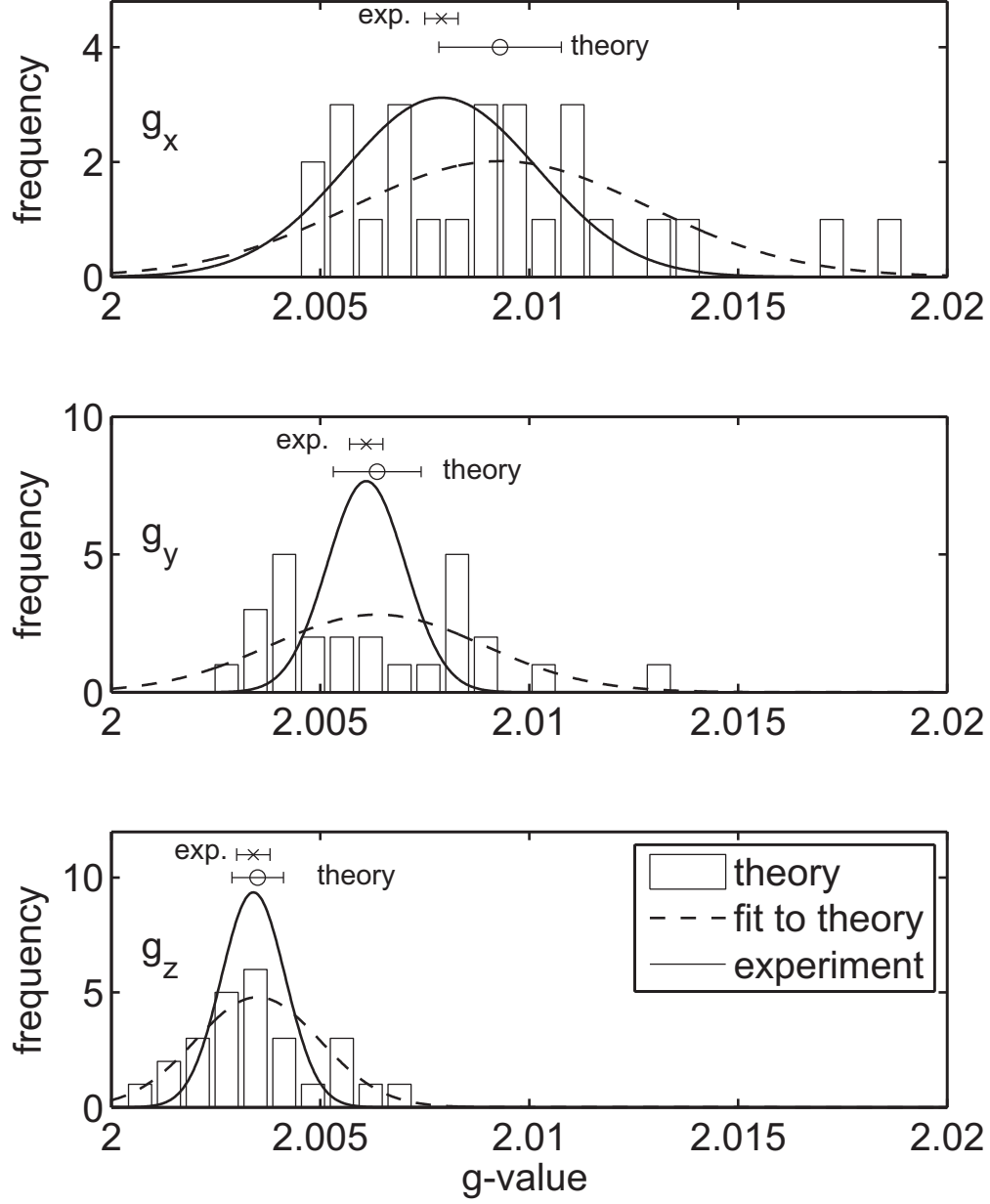


FIG. 3. Comparison between experimentally and theoretically (DFT) obtained principal g-values of coordination defects in a-Si:H. Values for different computer-generated DB models in a-Si:H are shown by the histogram. Principal values are sorted by size and assigned to g_x , g_y and g_z . The histogram was fitted by a normal distribution function shown by the dashed line. The experimental data for coordination defects obtained by a fitting model is shown by the solid line. The confidence intervals (2σ) of the mean experimental (cross) and theoretical (circle) principal values are shown separately to indicate their statistical significance.

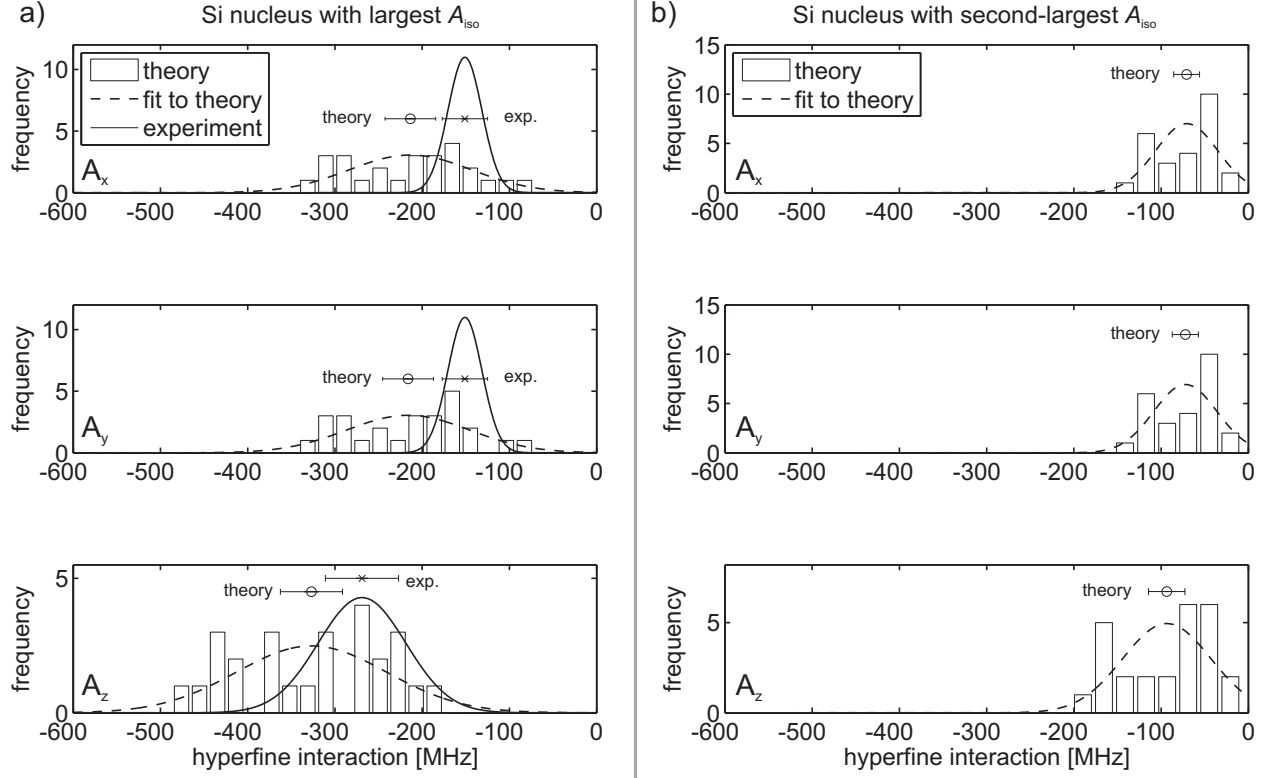


FIG. 4. Comparison between experimentally and theoretically (DFT) obtained principal values of the largest and second-largest HFI of coordination defects in a-Si:H. A-tensor of the ^{29}Si nucleus with the largest A_{iso} (a) and second largest A_{iso} (b). Values for different computer-generated models of a DB in a-Si:H are shown by the histogram. Principal values are sorted by size and assigned to A_x , A_y and A_z . The histogram was fitted by a normal distribution function shown by the dashed line. The experimental data for coordination defects obtained by a fitting model is shown by the solid line. The confidence intervals (2σ) of the mean experimental (cross) and theoretical (circle) principal values are shown separately to indicate their statistical significance.